Published in final edited form as:

Nat Struct Mol Biol. 2019 March ; 26(3): 175–184. doi:10.1038/s41594-019-0189-y.

Attenuated chromatin compartmentalization in meiosis and its maturation in sperm development

Kris G. Alavattam[1,2], **So Maezawa**[1,2,3], **Akihiko Sakashita**[1,2], **Haia Khoury**[4], **Artem Barski**[2,5], **Noam Kaplan**[4,*], and **Satoshi H. Namekawa**[1,2,*]

[1]Division of Reproductive Sciences, Division of Developmental Biology, Perinatal Institute, Cincinnati Children's Hospital Medical Center, Cincinnati, Ohio, 45229, USA

[2]Department of Pediatrics, University of Cincinnati College of Medicine, Cincinnati, Ohio, 49267, USA

[3]Department of Animal Science and Biotechnology, School of Veterinary Medicine, Azabu University, Sagamihara, Kanagawa 252-5201, Japan

[4]Department of Physiology, Biophysics & Systems Biology, Rappaport Faculty of Medicine, Technion - Israel Institute of Technology, Haifa, Israel

[5]Division of Allergy and Immunology, Division of Human Genetics, Cincinnati Children's Hospital Medical Center, Cincinnati, Ohio, 45229, USA

Abstract

Germ cells manifest a unique gene expression program and regain totipotency in the zygote. Here, we perform Hi-C analysis to examine 3D chromatin organization in male germ cells during spermatogenesis. We show that the highly compartmentalized 3D chromatin organization characteristic of interphase nuclei is attenuated in meiotic prophase. Meiotic prophase is predominated by short-range intrachromosomal interactions that represent a condensed form akin to mitotic chromosomes. However, unlike mitotic chromosomes, meiotic chromosomes display weak genomic compartmentalization, weak topologically associating domains, and localized point interactions in prophase. In postmeiotic round spermatids, genomic compartmentalization increases and gives rise to the strong compartmentalization seen in mature sperm. The X chromosome lacks domain organization during meiotic sex chromosome inactivation. We propose that male meiosis occurs amidst global reprogramming of 3D chromatin organization and that

*Corresponding authors: satoshi.namekawa@cchmc.org, noam.kaplan@technion.ac.il.
N.K and S.H.N are the co-senior authors of the article.

Author contributions

The manuscript was written by K.G.A., N.K., and S.H.N., with critical feedback from all other authors, and K.G.A and S.H.N. designed the Hi-C experiments. K.G.A and S.M. performed the Hi-C experiments. K.G.A., A.S., H.K., A.B., N.K., and S.H.N. designed and interpreted the computational analyses. K.G.A., A.S., H.K., and N.K. performed the computational analyses. N.K and S.H.N are the co-senior authors of the article.

Accession Codes

Hi-C data reported in this study were deposited to the Gene Expression Omnibus under accession no. GSE119805.

Competing Interest Statement

A.B. is a cofounder of Datirium, LLC.

strengthening of chromatin compartmentalization takes place in spermiogenesis to prepare the next generation of life.

Introduction

The germline is the sole lineage supporting the perpetuity of life. Its unique potential to recover totipotency is defined by chromatin mechanisms. Using genome-wide chromosome conformation capture (Hi-C), recent studies have suggested that sperm has highly compartmentalized 3D chromatin organization that resembles the interphase nuclei of embryonic cells[1-4]. This raises the possibility that some aspects of paternal chromatin organization may be predetermined in sperm prior to embryonic development.

The hallmark of germline development is meiosis, when the germ cell genome goes through recombination to facilitate genetic diversity in offspring[5,6]. In late spermatogenesis, germ cells undergo cellular reconstruction and global chromatin remodeling that ultimately gives rise to functional sperm[7]. Beginning in meiosis, global transcription networks are altered by the activation of germline-specific genes, and this process continues in postmeiotic spermatids[8-11]. As a result, the testis has the most diverse and complex transcriptomes of all organs[12]. However, it remains unknown how the spatiotemporal organization of germ cell chromatin facilitates vital gene expression programs and sets the epigenetic state for the next generation of life.

By performing Hi-C on representative stages of male germ cells from mice, we found that meiosis occurs amidst the attenuated compartmentalization of 3D chromatin organization; this compartmentalization is strengthened in haploid spermatids, giving rise to highly compartmentalized 3D chromatin organization in mature sperm. Our study suggests that the attenuated compartmentalization of 3D chromatin organization in male meiosis underlies complex germline transcriptomes and preparation for the next generation of life.

Results

The 3D chromatin organization of meiotic spermatocytes and postmeiotic spermatids

To determine the 3D chromatin organization of germ cells in late spermatogenesis, we isolated representative cell types from C57BL/6J mice and performed Hi-C experiments. Our analyses focused on pachytene spermatocytes (PS), which are in the midst of meiotic prophase and the synapsis of homologous chromosomes, and round spermatids (RS), which are haploid cells resulting from the second meiotic division (Fig. 1a). These two stages are accompanied by high levels of gene expression[9], last about a week each during spermatogenic differentiation, and represent a majority of testicular germ cells. We confirmed the high purity of isolated cells (Supplementary Fig. 1; Supplementary Dataset 1), which was consistent with our previous studies[11,13]. In addition to our processed Hi-C datasets (Supplementary Dataset 2; Methods), we reanalyzed a published dataset for mature sperm[2]. To provide a reference point for the analyses of spermatogenesis datasets, we also reanalyzed a mouse embryonic stem cell (ESC) dataset[14]. A recent study demonstrated that sperm has highly compartmentalized 3D chromatin organization that resembles the 3D

chromatin organization of ESCs[2]. Although it was not possible using these data to distinguish homologous chromosomes or sister chromatids characteristic of pachytene spermatocytes, we were able to evaluate the global features of 3D chromatin organization in each dataset.

First, we compared general features of pachytene spermatocyte genome organization with those of sperm and ESCs. Interaction maps of pachytene spermatocytes revealed atypical forms of higher-order chromatin organization in comparison to previous studies of interphase nuclei, sperm, and ESCs[14,15]. Consistent with the synapsis of homologous chromosomes and chromosome condensation, we detected an abundance of "near" intrachromosomal interactions (strong interactions along the diagonal of the "PS" panel in Fig. 1b) relative to sperm and ESCs. In this respect, pachytene spermatocyte chromosomes bore resemblance to somatic mitotic chromosomes (prometaphase mitosis human foreskin fibroblasts)[16] as well as the chromosomes of oocytes arrested in metaphase of meiosis II (MII oocytes)[3] (Supplementary Fig. 2a).

Next, we examined the intrachromosomal contact probability $P(s)$ for pairs of genomic loci stratified by genomic distance s, which may be indicative of the general polymer state of chromatin[17,18]. In sperm and interphase chromosomes, intrachromosomal contact probability has been reported to follow a power law of $P(s) \sim s^{-1}$, which could be consistent with a fractal globule state[17,18]. In contrast, the chromosomes in pachytene spermatocytes displayed a gradual decrease in intrachromosomal contact probability, following a power-law of $P(s) \sim s^{-0.61}$ at genomic distances up to 3 Mb (Fig. 1c), followed by a steep drop in contact probability at larger distances. Of note, the chromatin in pachytene spermatocytes bore resemblance to that observed in mitotic chromosomes. Consistent with previous studies[16,19], mitotic chromosomes displayed a power law decay of $P(s) \sim s^{-0.49}$ at distances up to 10 Mb, followed by a drop at larger distances; this has been suggested to be consistent with the presence of randomly anchored loop arrays[16,19]. The pachytene spermatocyte pattern also closely matched that observed for MII oocyte chromosomes: $P(s) \sim s^{-0.60}$ for distances up to 3 Mb, followed by a decrease (Fig. 1d). Together, these observations are in line with the overall condensed form shared by meiotic and mitotic chromosomes.

To investigate the dynamics of chromatin organization after meiosis, we studied Hi-C interaction maps of round spermatids. Round spermatid data were found to reflect an intermediate state between pachytene spermatocytes and mature sperm (Fig. 1b, c, e), with more long-range interactions than pachytene spermatocytes but less than sperm. Following round spermatids, mature sperm evinced highly compartmentalized 3D chromatin (Fig. 1b, e). These results suggest that the large-scale structure of meiotic chromosomes in pachytene spermatocytes resembles that of mitotic chromosomes, with round spermatid chromatin presenting an intermediate state towards mature sperm.

Attenuated compartmentalization of 3D chromatin organization in meiosis

Hi-C maps of interphase genomes often evince plaid patterns of chromatin interactions known as genomic compartments[17,20,21]. These have been interpreted as at least two alternating states of chromatin, A and B, in which each state preferentially interacts with other loci of the same state. Genomic compartments have been shown to be strongly

associated with biological features such as chromatin epigenetic state (A active/euchromatin; B inactive/heterochromatin) and gene expression (A expressed; B silenced). In order to accentuate genomic compartments, we normalized the intrachromosomal interaction maps by genomic distance and then calculated Pearson correlation matrices. In contrast to somatic mitotic chromosomes and MII oocytes, which do not show evidence of genomic compartments (Supplementary Fig. 2b)[3,4,16,19,22,23], we observed genomic compartments in both pachytene spermatocytes and round spermatids (Fig. 2a). Intriguingly, these compartments were attenuated relative to the compartments in sperm and ESCs (Fig. 2a).

Next, we sought to quantify the degree to which the genomic compartment signal appears in the data. Genomic compartments are usually detected by applying principal component analysis (PCA) to the aforementioned correlation matrices and extracting the first eigenvector (EV1), where the sign indicates the state (A/B) of each locus (Supplementary Dataset 3). However, PCA is not appropriate to quantify the degree of the compartment signal due to its relative sensitivity to noise and insensitivity to scale. Thus, we used a new approach to quantify the genomic compartment signal. Briefly, given some vector that indicates genomic compartment values (e.g., EV1), we selected loci with the highest 25% (strongest A) and lowest 25% (strongest B) of values, and calculated the strength of A-A and B-B interactions relative to A-B interactions (Methods). We refer to this quantity as "genomic compartment strength," and we verified that it can accurately quantify the degree of genomic compartment signal by mixing fixed proportions of the mature sperm Hi-C map, which shows strong genomic compartmentalization, with an interaction map that has no genomic compartments (Supplementary Fig. 3; Supplementary Dataset 3). Using this approach, we verified that the attenuated compartmentalization observed in pachytene spermatocytes is likely not due to contamination by heterogenous cells (Supplementary Fig. 1; Supplementary Dataset 1); further, we verified that genomic compartment strength in round spermatids indicates an intermediate status between pachytene spermatocytes and sperm (Fig. 2b). Finally, as expected, we found that genomic compartments, as captured by EV1 (Supplementary Dataset 3), are correlated with both gene expression (RNA-seq) and chromatin state (ChIP-seq) (Fig. 2c; Supplementary Fig. 4)[17]. Together, our data indicate that fundamental forms of genomic compartmentalization, similar to those found in interphase, are present but attenuated in male meiosis. These features are maintained and strengthened in the transition from meiotic to postmeiotic germ cells in spite of an overall dramatically different nuclear organization.

Interchromosomal interactions in late spermatogenesis

Next, we asked whether our Hi-C data recapitulate key features of chromosome organization during meiosis and in spermatids. In pachytene spermatocytes, homologous chromosomes have undergone synapsis, while chromosomes that are nonhomologous are separated from each other[24]. Consistent with the separation of nonhomologous chromosomes during prophase, we observed a low proportion of interchromosomal interactions in pachytene spermatocytes relative to sperm and ESCs (Supplementary Fig. 5; Supplementary Dataset 2). In order to accentuate interchromosomal interaction signals, we scaled the interaction matrix of each interchromosomal pair into a square matrix and calculated an average interchromosomal interaction frequency matrix over all such chromosome pairs (Methods).

We found frequent interchromosomal interactions between the acrocentric ends of chromosomes (telomeres proximal to centromeres) during meiosis as well as the interchromosomal association of non-centromeric ends (telomeres distal to centromeres) (Fig. 3a). These features may be due to the anchoring of telomeres to the nuclear membrane during meiosis (Fig. 3b). Studies utilizing microscopy demonstrated that, during meiotic prophase, both chromosome ends attach to the nuclear membrane[25] and, in particular, the acrocentric ends tend to associate because of the frequent association of pericentromeric heterochromatin[26]. Our Hi-C results are consistent with these microscopic observations.

This association of pericentromeric heterochromatin culminates in a single chromocenter in round spermatids, and this chromocenter persists into sperm (Fig. 1a). Consistent with this feature, we found that the acrocentric ends of chromosomes tended to associate in round spermatids and, to a lesser extent, in sperm (Fig. 3a and model shown in Fig. 3c; direct interactions between centromeres were not observed due to technical limitations related to sequencing highly repetitive regions of DNA). These general features were also observable, to a lesser degree, on an individual chromosome pair basis (e.g., chromosomes 2 and 4 in Fig. 3d), as were interchromosomal interactions of genomic compartments (Fig. 3d). Intriguingly, we observed the strongest interchromosomal interactions as those of genomic A compartments, which are gene-rich and abundant in active histone modifications (Fig. 2c), and which persist throughout spermatogenesis and in ESCs (Fig. 3d). And as with intrachromosomal interactions in round spermatids, we observed an increased proportion of interchromosomal interactions in round spermatids relative to pachytene spermatocytes (Fig. 3e). By measuring genomic compartment strength, we confirmed that interchromosomal genomic compartments are also present in pachytene spermatocytes (Fig. 3f). These results are surprising because they suggest that interactions associated with chromatin state are present between chromosomes in spite of their condensed form. Together, our data suggest that the observed interchromosomal interactions reflect key features of nuclear organization in spermatogenesis and that A compartments tend to self-associate between different chromosomes regardless of the stages of spermatogenesis (Fig. 3b, c).

Attenuated topologically associating domains in meiosis

In addition to genomic compartments, chromatin is spatially organized into regions of preferential interactions termed topologically associating domains (TADs)[14,15]. TADs have been implicated in the regulation of gene expression[15,27-29], and meiosis and subsequent stages are notable for their active transcriptomes, which are among the most complex and diverse known[12]. Thus, we identified TAD boundaries in late spermatogenesis with the software package HiCExplorer[30,31] (Methods; Fig. 4a; Supplementary Dataset 4). In pachytene spermatocytes and round spermatids, we observed weak, large TADs, ~1.1 Mb in average length (Fig. 4b; Supplementary Fig. 6; Supplementary Dataset 4). While many TAD boundaries were unique to each germ cell dataset (or shared between two of the three datasets), a subset of boundaries persisted from pachytene spermatocytes through to sperm (Fig. 4b, c): 622 TAD boundaries were common to pachytene spermatocytes (~27% of 2,300), round spermatids (~28% of 2,233), and sperm (~14% of 4,541). As late spermatogenesis progressed, the large TADs of pachytene spermatocytes and round spermatids underwent consolidation, forming an abundance of stronger, smaller TADs in

sperm, ~0.56 Mb in average length (Fig. 4b; Supplementary Fig. 6; Supplementary Dataset 4).

Consistent with these observations, the levels of distance-normalized chromatin interactions around sites of sperm TAD boundaries (±2 Mb) are higher in pachytene spermatocytes and round spermatids relative to sperm and ESCs (Fig. 4d: the baseline is above 1.0 in the “PS” and “RS” datasets). We further confirmed these data with 2D analyses of interaction frequencies in relative positions from start and end sites of sperm TAD boundaries (Fig. 4e). We detected weak structural features in pachytene spermatocytes and round spermatids ±0.5 Mb from the sites of sperm boundaries (Fig. 4f). This is in contrast to the sperm and ESC datasets, where chromatin interactions were largely restricted to within the sperm TAD boundaries (Fig. 4f). Interestingly, while a subset of weak TAD boundaries in pachytene spermatocytes were maintained as late spermatogenesis progressed, they did not become strengthened in sperm or ESCs (Supplementary Fig. 7). Taken together, these results suggest that many weak TAD boundaries apparent in meiotic spermatocytes are maintained in mature sperm, and additional alternative strong boundaries are gained.

Notably, in pachytene spermatocytes and round spermatids, the presence of common A/B compartments, along with large and weak TADs, evokes a chromosomal resemblance to paternal alleles in preimplantation development, which are in the midst of reprogramming of 3D chromatin organization[3,4,22]. Such features are distinct from those in somatic mitotic chromosomes and MII oocytes, which lack A/B compartments and TADs (Supplementary Fig. 2b)[3,4,16,19,22,23], thereby illuminating a chromatin configuration unique to meiotic chromosomes. This 3D chromatin status persists from meiotic prophase into round spermatids, which evince interphase-like nuclei following two rounds of reductional meiotic divisions. Through two successive rounds of meiotic divisions, chromosomes are condensed in two accompanying rounds of metaphase, during which 3D chromatin organization is presumed to have disappeared as is the case with mitotic chromosomes and MII oocytes (Supplementary Fig. 2b),[3,4,16,19,22,23]. Thus, these results may suggest that the epigenetic state of 3D chromatin organization is maintained through meiotic divisions.

Pairwise point interactions and active transcription during meiosis

Localized pairwise point interactions have been previously identified in high-resolution Hi-C interphase maps and have been associated with the activation of transcription and with gene-regulatory elements[32]. These point interactions are thought to arise from the clustering of regulatory elements and genes through chromatin looping mechanisms[32]. Chromosomes in meiotic prophase are distinct from those in mitotic M phase due to ongoing robust transcription. Thus, we examined the data for signs of such point interactions, both visually and computationally. We found that point interactions are clearly apparent in the data (Fig. 5a: dots shown with dashed circles and arrows) and, using the cLoops peak-calling package[33] with stringent statistical filtering (Methods), we identified 1,985 such point interactions genome-wide in pachytene spermatocytes (Supplementary Dataset 5). Next, we asked whether these point interactions are associated with specific genomic functions. We analyzed RNA-seq signals and the deposition of active histone modifications H3K27ac and H3K4me3, as well as silent histone modification H3K27me3, at the anchor sites of point

interactions (Supplementary Dataset 5). We found that, on average, anchors are enriched in H3K27ac and H3K4me3 ChIP-seq signals, as well as RNA-seq signal (Fig. 5b). Likewise, relative read enrichments for the histone and RNA-seq datasets were higher at anchors versus other regions of the genome (Supplementary Fig. 8a, b), and correlation calculations demonstrated a weak positive correlation between the anchors and the ChIP- and RNA-seq datasets (Supplementary Fig. 8c). It is interesting to note that the loci of point interactions appear to persist into round spermatids (Supplementary Fig. 8d); this is consistent with the overall similarity of transcriptomes in pachytene spermatocytes and round spermatids after the mitosis-to-meiosis transition of spermatogenesis[10]. Our data suggest that point interactions comprise a higher-order form of chromatin organization associated with active histone modifications and gene activation in late spermatogenesis.

Epigenetic mechanisms associated with 3D chromatin organization in the germline

This led us to an intriguing question: How does the higher-order organization of pachytene spermatocytes and round spermatids relate to the formation of TADs in sperm? To seek an answer, we analyzed the deposition of H3K27ac, H3K4me3, and H3K27me3 at sites of sperm TAD boundaries (Supplementary Dataset 4) across the four datasets. Surprisingly, we observed the strong enrichment of H3K27ac, H3K4me3, and H3K27me3 at the sites of sperm TAD boundaries in pachytene spermatocytes and round spermatids (Fig. 5c), indicating that sperm TAD boundaries are delineated with epigenetic marks as early as the pachytene spermatocyte stage. The enrichment of histone modifications at sperm TAD boundaries was also present in ESCs (Fig. 5d). These results raise the possibility that epigenetic mechanisms, which persist through meiotic divisions, determine 3D chromatin organization in the germline. In the germline, bivalent genomic domains that retain both H3K4me3 and H3K27me3 on gene regulatory elements are postulated to be responsible for epigenetic inheritance across generations[13,34]. Therefore, such mechanisms could serve as persistent memories through meiotic divisions. In support of this notion, from pachytene spermatocytes through to sperm, H3K27me3 is enriched in A compartments, which are also enriched with H3K4me3 (Fig. 2c; Supplementary Fig. 4).

3D chromatin organization of the XY body during meiosis and postmeiotic sex chromatin in round spermatids

Next, we shifted our attention from autosomal chromatin organization to chromatin organization of the X chromosome. In pachytene spermatocytes, the sex chromosomes undergo a phenomenon known as meiotic sex chromosome inactivation (MSCI) and form a transcriptionally silent compartment termed the XY body (also known as the sex body)[35]. MSCI begins when DNA damage signaling recognizes the unsynapsed status of the hemizygous X and Y chromosomes, resulting in their transcriptional repression[36]. Consistent with the distinct regulation of the sex chromosomes in the XY body, interaction maps of pachytene spermatocytes revealed that X evinces chromatin organization that is highly—but not entirely—homogenous (Fig. 6a-c; Supplementary Fig. 9), without chromatin compartments (Fig. 6a-c). In this respect, the pachytene spermatocyte X closely resembles the MII oocyte X (Supplementary Fig. 9a, b). Interestingly, the chromatin features of the inactive X chromosome in meiosis are distinct from those of the inactive X chromosome in female X chromosome inactivation. In female X chromosome inactivation,

X is folded into two "megadomains"[32,37-39] that are established via a step-wise mechanism[40]. However, the silent male X in meiosis does not have apparent megadomains (Fig. 6a). This could be explained by the mechanistic difference between male and female inactive X chromosomes: The male inactive X is established via DNA damage signaling, while the female inactive X is established through the action of non-coding *Xist* RNA[36,41].

The distinct regulation of the sex chromosomes persists into postmeiotic round spermatids, where either X or Y is organized into a silent compartment, termed postmeiotic sex chromatin (PMSC), in the center of the nucleus (Fig. 1a)[9]. Intriguingly, we observed the beginnings of higher-order chromatin organization in RS in the form of distal interactions greater than 10 Mb (Fig. 6b); however, as in pachytene spermatocytes, round spermatids lacked chromatin compartmentalization in PMSC (Fig. 6c, d). In support of these results, by measuring genomic compartment strength, we confirmed that intrachromosomal genomic compartments are infrequent on the X chromosome in pachytene spermatocytes and round spermatids (Fig. 6e). In round spermatids, a small number of sex-linked genes escape postmeiotic silencing to spur differentiation into sperm[9,42]. However, these escape genes did not demonstrate apparent features of 3D chromatin organization in round spermatids (Supplementary Fig. 9c). By the time germ cells progressed to sperm, higher-order features of chromatin organization, such as compartments, were observable (Fig. 6a-d; Supplementary Fig. 9c). The overall features of the sperm X resemble those of the active X in ESCs, especially with respect to multi-domain organization (Fig. 6a)[2], while compartments are distinct between the sperm X and the active X in male ESCs, which is of maternal origin (Fig. 6c, d). Together, our data implicate 3D chromatin organization in the distinct regulation of the sex chromosomes in germ cell development.

Discussion

In this study, we revealed a form of 3D chromatin organization predominated by local, weakly preferential chromatin interactions in meiotic prophase that expand to distal, although still weakly preferential, interactions in postmeiotic spermatids. These features present intriguing clues to understand the structure of meiotic chromosomes in prophase. Through microscopy of mammalian cells, chromatin loop array structures in meiotic prophase were reported to be similar to mitotic counterparts[43], which an earlier Hi-C study modeled as compressed arrays of consecutive loops[16]. However, to date, 3D structural information is lacking in mammalian meiotic prophase. In yeast, chromosome conformation capture (3C), the pioneering method that underlies Hi-C, provided keen structural insights into meiotic chromosomes[44], and recent yeast Hi-C studies demonstrated that meiotic chromosomes are comprised of dense, dynamic arrays of chromatin loops with variable sizes[45,46]. However, in comparison to other eukaryotes, yeast chromosomes do not display some features of higher-order chromatin organization, such as A/B compartments [47-49], thereby precluding direct comparisons between yeast and mammalian meiotic chromosomes. Here, we show that mammalian meiotic chromosomes evince atypical features of higher-order chromatin organization: In comparison to somatic interphase chromosomes[14,17,21,23], the chromosomes of pachytene spermatocytes feature relatively attenuated structural features. One interpretation may account for this: Since our Hi-C data for pachytene spermatocytes represent the average structural features from ~25 million

nuclei (each nucleus with two complements of the diploid genome), loop positions may be random in the cell population and loop sizes may be variable.

Nonetheless, in comparison to mitotic chromosomes, pachytene spermatocyte chromosomes displayed a steeper decrease in intrachromosomal contact probability (Fig. 1d), in addition to genomic compartmentalization (Fig. 2) and the presence of TADs (Fig. 4). So, it is intriguing to consider structural influences acting on the chromosomes of pachytene spermatocytes. Mechanistically, the structural features of meiotic chromosomes may be shaped by the meiosis-specific effects of cohesins and CTCF, which define 3D structural organization in interphase nuclei[50-52]. During meiosis, chromosome axes are ubiquitously loaded with meiosis-specific cohesins[53], and CTCF has an isoform unique to meiosis and subsequent stages, BORIS[54]. Thus, these factors may function in mechanisms that randomize loop positions.

After our analyses of meiotic chromosomes, the observations of patterns found in mitotic and interphase chromosomes raise interesting questions: For example, what physical genome structures are consistent with both the randomized loop arrays proposed for mitotic chromosomes and the consistent structural features typically found in interphase chromosomes? How is genomic organization functional in spite of its attenuated form? And how do condensed chromosomes form interchromosomal interactions between active chromatin loci (Fig. 3)?

Although the features of chromatin loop arrays—random and/or structured—may be shared between autosomes and sex chromosomes during meiosis, we determined additional and unique structural features related to the inactive sex chromosomes in the male germline. Phase separation, a process by which membraneless organelles form and behave as liquid droplets[55,56], has been proposed as a mechanism for the formation of heterochromatin[57,58]. Furthermore, a phase separation mechanism was postulated for the stepwise establishment of the inactive X in females[40]. Given the highly homogenous and isolated 3D chromatin organization of the inactive X in late spermatogenesis, the XY body and PMSC may represent droplet-like structures that are self-associating and spatially segregated via phase separation mechanisms. Furthermore, phase separation mechanisms also underlie sites of active transcription[59]. Therefore, it is tempting to speculate that phase separation mechanisms may underlie interchromosomal association mediated through A compartments.

In 1984, Robin Holiday proposed, in an article entitled “The biological significance of meiosis,” that a potential function of meiosis is the reprogramming of gametes to prepare for the next generation[60]. In accordance with this hypothesis, we propose that attenuated compartmentalization of 3D chromatin organization in meiosis is itself a form of reprogramming for 3D chromatin organization that facilitates spermatogenic gene expression. Moreover, the attenuated compartmentalization of 3D chromatin organization corroborates the reorganization of various chromatin features in the mitosis-to-meiosis transition of the male germline[10,11,13]. In summary, our results reveal that the attenuated compartmentalization of germline chromatin is associated with unique and diverse transcriptomes, and that the maturation of germline chromatin to highly compartmentalized 3D chromatin organization in sperm prepares the next generation of life.

Methods

No statistical methods were used to predetermine sample sizes. No data were excluded from analyses. The experiments were not randomized, and, except where noted, investigators were not blinded to allocation during experiments and outcome assessment.

Animals and germ cell isolation.

Wild-type C57BL/6J mice were used for Hi-C analyses, and all experimental work was approved by the Institutional Animal Care and Use Committee, protocol no. IACUC2015–0032.

Pachytene spermatocytes (PS) and round spermatids (RS) were isolated from adult testes through sedimentation velocity at unit gravity as described[61]. At least 12 independent mice, at 90 to 120 days of age, were used for each isolation of germ cells. Purity was confirmed via fluorescence wide-field microscopy: All images were acquired with an ECLIPSE Ti-E microscope (Nikon) and Zyla 5.5 sCMOS camera (Andor Technology), with a 60x CFI Apochromat TIRF oil immersion lenses (Nikon), numerical aperture 1.40. Germ cells were identified by staining with 0.2 μg/ml Hoechst 33342. In keeping with previous studies from the Namekawa lab[62-64], mean purity of ≥91% for pachytene spermatocytes and ≥94% for round spermatids was confirmed for each experiment (Supplementary Fig. S1; Supplementary Dataset S1). To quantify the purity of isolated germ cells, images of cell fractions from sedimentation velocity at unit gravity, their details having been blinded, were fed into a partially automated Fiji/ImageJ[65,66] processing pipeline. Using a Gaussian filter, the images were smoothed before applying a pixel intensity maximum filter to identify local maxima, which were automatically scored as cells. Then, each processed image was checked manually to correct for false positives and false negatives. Unprocessed versions of the blinded images were manually checked for heterogeneous cell contamination. Percent contamination was calculated for given sets of images as follows: $\left(\frac{number\ of\ heterogenous\ cells}{corrected\ totoal\ number\ of\ cells}\right) \times 100$. The details of the processed and unprocessed versions of the images were unblinded, and sample purity for each fraction was calculated by subtracting the percent contamination for a given image from 100%. For both pachytene spermatocytes and round spermatids, two independent biological replicates were generated for Hi-C library preparation and sequencing (Supplementary Dataset S2).

Hi-C: Library generation and sequencing.

To generate and sequence Hi-C libraries, Hi-C was performed as described[67] with the following details and additions: Samples were treated with HindIII restriction enzyme and, for DNA sequencing, NEBNext Oligos for Illumina, Index Primer Set 1, were used. To ensure high library complexity[68,69], each of two independent biological replicate libraries for pachytene spermatocytes, which have two complements of the diploid genome, were generated from 12.5 million cells (150-bp paired-end sequencing); and each of two biological replicate libraries for round spermatids, which have haploid genomes, were generated from 50 million cells (75-bp and 100-bp paired-end sequencing). All libraries were sequenced on either Illumina HiSeq2500 or HiSeq4000 sequencers according to the manufacturer's instructions.

Hi-C: Sourcing, alignment, and processing.

Hi-C datasets not generated in this study were obtained from published work (as listed in Supplementary Dataset 2): sperm (50-bp paired-end reads; PMID 28178516, GEO GSE79230)[70], embryonic stem cells (ESCs; 75-bp paired-end reads; PMID 24185094, GEO GSE48592)[71], non-synchronized human foreskin fibroblasts (HFF1-non-synchronized; 50-bp paired-end reads; PMID 24200812, ArrayExpress E-MTAB-1948)[72], synchronized prometaphase mitosis human foreskin fibroblasts (HFF1-mitosis; 50-bp paired-end reads; PMID 24200812, ArrayExpress E-MTAB-1948)[72], and metaphase meiosis II oocytes (MII oocytes; 150-bp paired-end reads; PMID 28703188, GEO GSE82185)[73].

Paired-end .fastq files of Hi-C libraries were mapped and processed using the cMapping package as described previously[69,74]. Matrix binning and balancing was performed with the Cooler software package[75] (version 0.7.6 or 0.7.10). In brief, paired-end reads were iteratively mapped to the *Mus musculus* mm10 genome via Bowtie2 (version 2.3.3.1)[76], which was called with the following arguments: --very-sensitive --no-head --no-sq --qc-filter --reorder. Uniquely aligned, paired reads were kept and assigned to the 5' position of HindIII restriction fragments. Mapped reads were filtered for fragment ends and uniqueness; PCR duplicates, defined as sequence matches with the exact same start and end, were excluded. Using the Cooler package, the valid pairs were binned at the following resolutions (kb): 1, 2, 5, 8, 10, 15, 20, 30, 40, 64, 100, 128, 250, 256, 512, 1024, 2048, 4096, and 8192. To correct for noisy and/or low-signal bins prior to matrix balancing, bins with coverage ≤20 genome-wide median deviations below the median bin coverage were excluded. Finally, matrices were balanced using Sinkhorn balancing such that the sum of every row and column is equal[74].

The alignment and processing pipeline resulted in 284.9 million unique, valid read pairs for pachytene spermatocytes (replicates pooled); 415.6 million unique, valid read pairs for round spermatids (replicates pooled); 371.0 million unique, valid read pairs for sperm (replicates pooled); 625.8 million unique, valid read pairs for embryonic stem cells (replicates pooled); 113.7 million unique, valid read pairs for non-synchronized human foreskin fibroblasts; 83.5 million unique, valid read pairs for synchronized prometaphase mitosis human foreskin fibroblasts; and 695.0 million unique, valid read pairs for metaphase meiosis II oocytes (replicates pooled; Supplementary Dataset 2). Processed, pooled Hi-C datasets were used for all experiments. To minimize the potential effects of variable sequencing depths when making comparisons between the datasets, processed, pooled Hi-C datasets for pachytene spermatocytes, round spermatids, sperm, embryonic stem cells, and metaphase meiosis II oocytes were randomly sampled to 280 million read pairs and then balanced via Sinkhorn balancing as described above; for non-synchronized human foreskin fibroblasts and synchronized prometaphase mitosis human foreskin fibroblasts, processed, pooled Hi-C datasets were randomly sampled to 83.5 million read pairs and then balanced via Sinkhorn balancing.

Hi-C: Analyses of intrachromosomal interaction matrices and differential interactions between samples.

To generate and visualize interaction frequency heatmaps of whole chromosomes, Hi-C matrices at 100-, 128-, or 250-kb resolution were imported to the software package HiCExplorer[77,78] (version 2.1.3 cooler_correction_patch) for use with the application hicPlotMatrix. To aid visual comparisons between the datasets, matrices were natural log transformed. To analyze differential interaction frequencies between samples, the HiCExplorer application hicCompareMatrices was used to generate $\log_2$ ratios of interaction frequency matrices between two separate datasets.

Hi-C: Estimation of power-law coefficients for interaction frequency curves:

To estimate the power-law decay coefficients of interaction frequency versus genomic distance, we used a maximum likelihood approach[79,80]. Specifically, we assumed that the probability of interaction between loci i and j are given by $P_{int}(i,j) = z|i-j|^{\alpha}$, where z is a normalization factor to ensure a probability distribution. Next, we assumed a Hi-C experiment can be described as multinomial sampling from the above probability distribution. Therefore, the likelihood of observing Hi-C matrix X is $P(X \mid \alpha) = [\frac{!\sum X_{i,j}}{\prod(!X_{i,j})}]\prod_{i,j}(z \mid i-j \mid^{\alpha})^{X_{i,j}}$. We then used SciPy LM-BFGS quasi-Newton optimization[81] to find the α value that maximizes the likelihood. Since, in some cases, the data adhere to regimes with different power-laws, we selected an appropriate range of genomic distances that were used to estimate α as follows: pachytene spermatocytes, 0.5-3 Mb; MII oocytes, 0.5-3 Mb; HFF1-mitosis, 0.5-7 Mb.

Hi-C: A/B compartment analyses.

Hi-C matrices at 100- or 128-kb resolution were imported to HiCExplorer[77,78] (version 2.1.3 cooler_correction_patch) for use with the applications hicTransform and hicPlotMatrix. hicTransform was called to convert interaction frequency matrices to distance-normalized matrices (i.e., matrices taken from dividing observed interactions by expected interactions as described[82]), then to subsequently generate Pearson correlation coefficient matrices. hicPlotMatrix was used to visualize the Pearson correlation coefficient matrices.

To call genomic compartments, the HiCExplorer application hicPCA was employed to perform principal component analysis (PCA) on Pearson correlation coefficient matrices at 100- or 128-kb resolution (Supplementary Dataset S3). The largest eigenvector (EV1) represented the genomic compartment profile, which is consistent with previous reports[82-84]. For confirmation, consecutive eigenvectors were evaluated; eigenvectors beyond EV1 represented profiles distinct from genomic compartments (data not shown). Per convention, genomic compartments were assigned one of two designations, ‘A’ (active/euchromatic compartments) and ‘B’ (inactive/heterochromatic compartments), based on associated biological features, including gene density, mRNA transcription, and markers of chromatin state such as histone post-translational modifications. In comparison to B compartments, A compartments were denoted by higher gene densities (data not shown), increased enrichment for mRNA transcription, and increased enrichment of H3K27ac and H3K4me3, post-

translational modifications conventionally associated with euchromatin and active transcription.

Hi-C: Evaluation of genomic compartment strength.

To evaluate the level of genomic compartmentalization between datasets, a new approach that calculates the "genomic compartment strength" was developed due to the limitations of PCA for this task. This approach quantifies the genomic compartment signal by examining the level of interaction in regions belonging to the same compartment versus regions belonging to different compartments. The definition of compartments is given by an eigenvector as explained in the preceding section; the choice of this vector is independent from the rest of the analysis. Then, we selected the highest 25% and lowest 25% of values, which indicate, respectively, strong A and strong B loci. Next, a Hi-C interaction matrix was distance-normalized by taking the $log(\frac{observed\ interactions}{expected\ interactions})$; the resulting normalized matrix was referred to as a "LOE" matrix. Then, genomic compartment strength was defined as $mean(AA\ LOE\ interactions) + mean(BB\ LOE\ interactions) - 2[mean(AB\ LOE\ interactions)]$. Thus, if AA and BB interactions were stronger than AB interactions, a positive value was expected; if AA and BB interactions were equivalent to AB interactions, then a value close to zero was expected.

Hi-C: Genomic compartment strength analysis in a controlled setting.

In order to test whether genomic compartment strength analysis accurately quantifies changes in compartment strength, different portions of the sperm Hi-C matrix S (which has the highest GC strength) were mixed with a matrix M that does not have any genomic compartments. Matrix M was constructed by taking the pachytene spermatocyte interaction frequency map and converting it to an expected interaction map such that the interaction probability at distance x is the average interaction probability of all loci within that distance. It was verified that M has a genomic compartment strength of approximately zero. To obtain a mixed matrix with sperm mixed fractions f is [0, 0.1, 0.2, 0.3, 0.4, 0.5, 0.6, 0.7, 0.8,0.9, 1.0] we sampled $f \times sum(PS)$ reads multinomially according to the probabilities given by matrix S, and combined these with $(1-f) \times sum(PS)$ reads sampled multinomially by the probabilities of matrix M. We created mixed matrices at controlled levels, where f is [0, 0.1, 0.2, 0.3, 0.4, 0.5, 0.6, 0.7, 0.8,0.9, 1.0], and genomic compartment strength was calculated for each such matrix, both for cis and trans interactions. To avoid eigenvector distortion resulting from weak compartment signals, all mixed samples used the eigenvector extracted from S. To account for randomness introduced by sampling, we repeated this analysis 10 times and calculated the mean and standard deviation of the genomic compartment strength at each value of f (Supplementary Dataset S3). We observed that genomic compartment strength is sensitive to detect differences between the matrices and scales nearly linearly at ranges 0.2–1.0 (Supplementary Fig. S3).

Next, we asked whether the relatively weak genomic compartment strength observed in pachytene spermatocytes and round spermatids can be entirely due to contamination by a small fraction of cells that have strong compartmentalization. By comparing the observed genomic compartment strengths of pachytene spermatocytes and round spermatids to the

calibration curve, we found that the pachytene spermatocyte samples would need to be contaminated by ~22% cells with strong compartmentalization to reach the observed genomic compartment strength; round spermatid samples would need to be contaminated by ~55% cells with strong compartmentalization (Supplementary Fig. S3). Since the mean contamination of pachytene spermatocytes is ≤9% and the mean contamination of round spermatids is ≤6% (Supplementary Fig. S1), these results suggested that the observed compartmentalization is likely not due to contamination. The analysis was performed with interaction matrices at 1024-kb resolution. Similar results were obtained with different matrix resolutions.

Hi-C: Evaluation of interchromosomal interactions.

Given a Hi-C matrix at 1024-kb resolution, an interchromosomal submatrix was taken for each pair of different chromosomes and rescaled into a matrix of size 500 × 500 bins. Each chromosome pair submatrix was taken in both orientations. Next, an average interchromosomal matrix was calculated by taking the average of all submatrices. Finally, the matrix was normalized by dividing each entry by the matrix mean and then taking the natural logarithm. Similar results were obtained with different matrix resolutions.

For analyses of interchromosomal interaction frequencies between two separate chromosomes, and for analyses of combined, genome-wide intra- and interchromosomal interactions, Hi-C matrices at 250-kb resolution were imported to HiCExplorer[77,78] (version 2.1.3 cooler_correction_patch) for use with the application hicPlotMatrix. Resulting data were natural log transformed to aid visual comparisons between the datasets.

Hi-C: Identification and visualization of topologically associating domains (TADs).

Hi-C matrices were imported to HiCExplorer[77,78] (version 2.1.3 cooler_correction_patch) for use with the applications hicFindTADs and hicPlotTADs. hicFindTADs identifies TAD boundaries through an approach that calculates “TAD separation scores”[77,85]. Briefly, for each dataset, interaction frequency matrices at 20-kb resolution were transformed into z-score matrices based on the distribution of contacts at given genomic distances. Then, for a given bin of a z-score submatrix, the contacts between an upstream and downstream region of width w were calculated, thereby generating a TAD separation score; to reduce noise, multiple values were used for w and averaged per bin. Genomic bins with low TAD separation scores relative to neighboring regions were defined as local minima and called as TAD boundaries; stronger boundaries possessed lower TAD separation scores. Statistical significance was estimated for each local minimum by comparing the distribution of z-scores for submatrices, and the Wilcoxon rank sum test was used to compare the values. The false-discovery rate (FDR) was used to correct p values; the FDR q value threshold was set to 0.01. A thorough explanation for how hicFindTADs functions, including examples of utilization, is available in PMID 29335486[77] as well as the online documentation for HiCExplorer (http://hicexplorer.readthedocs.io/en/latest/content/tools/hicFindTADs.html#hicfindtads). hicFindTADs was called on all processed, pooled Hi-C matrices with the following arguments (all other arguments were set to default parameters): --minDepth 80000 --maxDepth 800000 --step 40000 --minBoundaryDistance 80000 --correctForMultipleTesting fdr --thresholdComparisons 0.01 --delta 0.01.

The output of hicFindTADs includes lists of TAD separation scores (Supplementary Dataset S4), and these were imported to the application hicPlotTADs in order to plot regions along the diagonals (i.e., the linear DNA) of interaction frequency matrices in combination with TAD boundary start and stop positions, which were also output by hicFindTADs. In addition, lists of TAD separation scores and positions were used to calculate and graph various TAD metrics for the individual datasets (e.g., Figs. 4a, c; Supplementary Fig. S6; Supplementary Dataset S4).

Hi-C: Evaluation of TAD boundary intersections.

To compare the intersections of TAD boundaries between pachytene spermatocytes, round spermatids, and sperm, we culled 1-bp TAD boundary positions using .bed output from hicFindTADs (Supplementary Dataset S4). However, because hicFindTADs was run on interaction frequency matrices at 20-kb resolution (i.e., binned in 20-kb windows), these data cannot call boundary positions with the accuracy of 1 bp; to account for this, we took the 1-bp TAD boundary positions ± 30 kb (i.e., 60 kb centered on each boundary) for subsequent analyses. The TAD boundary positions ± 30 kb were saved in .bed files (Supplementary Dataset S4) and fed into the command line program Intervene[86]. Intervene was set to call the R package UpSetR[87], which visualizes intersections in a matrix layout, grouping datasets based on the presence and/or absence of intersections. An example command line call for the evaluation of TAD boundary intersections: $ intervene upset -i *$PS_bed_30kb $RS_bed_30kb $sperm_bed_30kb*.

Hi-C: Evaluation of interaction frequencies between TAD boundaries.

For each intrachromosomal matrix, we normalized each 2d bin *b* by dividing its value by the average value of all bins in its diagonal and taking the natural logarithm of the result. Next, for each pair of TAD boundaries, we extracted from the normalized matrix a 51×51 submatrix at 20-kb resolution, centered on the intersection of the boundaries. Then, we calculated the average over all submatrices. For this analysis we used only data within diagonals 3–500 (i.e., genomic distances of 60 kb to 10 Mb) of the normalized matrix.

To compute 2D line plots depicting interaction tendencies 0 to ±2 Mb from TAD boundaries (Fig. 4d and Supplementary Fig. S7a), distance-normalized submatrices (observed interactions/expected interactions), derived from Hi-C interaction frequency matrices at 20-kb resolution, were called with the HiCExplorer[77,78] (version 2.1.3 cooler_correction_patch) application hicAggregateContacts. In brief, submatrices centered at the intersections of TAD boundary start and end regions were selected, and all interactions from 0 to ±2 Mb of the boundaries were considered. These interactions were split over 100 bins from the center of the submatrix in the horizontal and vertical directions. Then, the submatrices were pooled by computing their averages at all positions. The interaction frequencies of the averaged submatrices were normalized by dividing individual values by the total interaction frequencies in the submatrix. Then, the diagonal, from top left to bottom right, of the pooled, averaged submatrix was output as a 2D line plot. hicAggregateContacts was called with the following arguments: --avgType mean --transform obs/exp --range 20000:2020000 --numberOfBins 100 --plotType 2d --diagnosticHeatmapFile $*basefile_description_date.svg* --howToCluster diagonal --kmeans 1.

Hi-C: Identification of pairwise point interactions in pachytene spermatocyte chromosomes.

Pairwise point interactions were called on pachytene spermatocyte data using the software package cLoops (version 0.9)[88] as follows: $ cLoops -f *$file_bedpe* -o *$output_hic* -s -eps 10000,15000,20000,25000 -minPts 10,20,30,40,50 -hic. We identified 12,990 significant point interactions. However, manual assessment of the results indicated that a majority of these could either not be confirmed visually or were not found in both replicates. We therefore reduced the set into a high-confidence set of 1,985 point interactions (Supplementary Dataset S5), which better matched visual assessment and was more consistent between replicates. To reduce the set, we selected only significant point interactions with a binomial p value <1e-10. We found that this filtered set of point interactions was also consistent with an independent peak-calling method based on signal-processing filters (data not shown).

RNA-seq and ChIP-seq: Sourcing, alignment, processing, and visualization.

RNA-seq and ChIP-seq datasets were obtained from published work: for RNA-seq, pachytene spermatocytes and round spermatids (PMID 25703348, GEO GSE55060)[62], sperm and embryonic stem cells (PMID 22242016, DDBJ DRA000484)[89]; for ChIP-seq of H3K27ac, pachytene spermatocytes and round spermatids (PMID 29462142, GEO GSE107398)[90], sperm (PMID 28178516, GEO GSE79230)[70], and embryonic stem cells (PMID 22763441, GEO GSE29218)[91]; for ChIP-seq of H3K4me3, pachytene spermatocytes and round spermatids (PMID 25703348, GEO GSE89502)[62], sperm (PMID 28178516, GEO GSE79230)[70], and embryonic stem cells (PMID 22763441, GEO GSE29218)[91]; for ChIP-seq of H3K27me3, pachytene spermatocytes and round spermatids (PMID 25703348, GEO GSE89502)[62], sperm (PMID 28178516, GEO GSE79230)[70], and embryonic stem cells (PMID 25303531, GEO GSE57912)[92].

For RNA-seq analyses, .fastq files were aligned to the *Mus musculus* mm10 reference genome via Spliced Transcripts Alignment to a Reference (STAR; version 2.4.2a)[93], and only unique alignments were allowed with a maximum of two errors per alignment. For ChIP-seq analyses, .fastq files were aligned to the *Mus musculus* mm10 reference genome with Bowtie[94] (version 1.1.1), and only unique alignments were allowed with a maximum of one error per alignment. To estimate fragment sizes, and to find islands of enrichment, MACS2[95] (version 2.1.0.20140616) was used with an FDR q value threshold of <0.2.

RNA- and ChIP-seq datasets were processed and visualized through one of two pipelines: (1) the BioWardrobe Experiment Management Platform[96], which indexes and normalizes .bam files, makes use of NCBI RefSeq annotation to categorize reads from .bam files, and then, for viewing, uploads the data to the UCSC genome browser[97]; and (2) the deepTools[98] (version 3.1.0) application bamCoverage, which was used to normalize indexed .bam files and bin resulting values in 50-bp windows; then, the output of bamCoverage was imported to HiCExplore (version 2.1.3 cooler_correction_patch)[77,78] for visualization via the applications hicPlotMatrix and hicPlotTADs.

RNA- and ChIP-seq enrichment with respect to TAD boundaries, genomic compartments, and point interaction anchor centers.

Using sorted .bam files and the software package ngsplot (version 2.6.3)[99], we calculated the enrichment of RNA-seq data and/or ChIP-seq data for histone post-translational modifications with respect to EV1 lists (Supplementary Dataset S3), TAD boundary lists (Supplementary Dataset S4), and lists of point interaction anchor centers (Supplementary Dataset S5). An example command line call for point interaction anchor centers: $ ngs.plot.r -G mm10 -R bed -C *$configuration_file* -O *$output_file* -SE 0 -FL 400 -L 1000000.

RNA- and ChIP-seq read enrichment (CPM) at pairwise point interaction anchors.

Using .bedpe files output by cLoops (version 0.9)[88], we generated a .bed file containing genomic location information for individual pairwise point interaction anchors on pachytene spermatocyte chromosomes (Supplementary Dataset S5). Using the program bedtools (version 2.27.1)[100] and its application intersect, we also generated a .bed file for all genomic regions excluding point interaction anchors. Then, we calculated read enrichment for ChIP- and RNA-seq data at anchor or anchor-excluded (i.e., "other") genomic regions using bedtools intersect, e.g., $ bedtools intersect -c -a *$bed_file_for_regions* -b *$sorted_bam_file_for_NGS_data* > *${sorted_bam_file_for_NGS_data %.bam}_reads_enrichment_at_regions.txt*. Resulting regional read enrichment was normalized for sequencing depth using a counts per million (CPM) calculation, i.e., uniquely mapped reads were scaled by the total number of sequenced reads multiplied by 1,000,000: $regional\ read\ enrichment \times \left(\frac{1}{total\ number\ of\ sequenced\ reads} \times 1,000,000\right)$. To test for statistical differences between read enrichment at "anchor" versus "other" regions, we performed Wilcoxon rank sum tests with Bonferroni post corrections.

RNA- and ChIP-seq enrichment correlation with pairwise point interactions.

The pairwise point interaction anchor .bed file (Supplementary Dataset S5) was converted to a .bam file through the bedtools (version 2.27.1)[100] application bedtobam. Then, we employed the software package deepTools[98] (version 3.1.0) application multiBamSummary to stratify the anchor, RNA-, and ChIP-seq .bam files in 40-kb bins and calculate the genome coverage for each bin. Resulting coverage matrices were processed with the deepTools application plotCorrelation in order to compute the Pearson and Spearman correlation coefficients, and to visualize the correlation calculation results as hierarchically clustered heatmaps.

Figure preparation.

Plots were generated with, alone or in combination, Excel (2013, Microsoft), the R software package ggplot2 (version 3.1.0)[101], and the various plotting programs employed by the other software packages used in this study. Illustrator (CS6, Adobe) was used for composing figures.

Code availability.

Source code for all software used in this study, with documentation, examples, and additional information, is available at the following URLs:

- https://github.com/dekkerlab/cMapping
- https://github.com/mirnylab/cooler
- http://bowtie-bio.sourceforge.net/bowtie2
- https://github.com/deeptools/HiCExplorer
- https://github.com/asntech/intervene
- https://github.com/hms-dbmi/UpSetR
- https://github.com/YaqiangCao/cLoops
- https://github.com/alexdobin/STAR
- http://bowtie-bio.sourceforge.net/
- https://github.com/taoliu/MACS
- https://github.com/deeptools/deepTools
- https://github.com/arq5x/bedtools2
- https://github.com/shenlab-sinai/ngsplot
- https://github.com/tidyverse/ggplot2

Other code used in this study, including code for compartment strength analysis and code for average trans interaction analysis, is available at https://github.com/KaplanLab/Spermatogenesis. A version of HiCExplorer that includes the cooler_correction_patch branch is forked at https://github.com/NamekawaLab/HiCExplorer. Any further code is available upon request. Information for the BioWardrobe Experiment Management Platform[96], which is commercial software, is available at https://biowardrobe.com and https://github.com/Barski-lab/biowardrobe.

Data availability statement

All Hi-C sequencing data used in this study, including processed files for published datasets, have been deposited in the National Center for Biotechnology Information (NCBI) Gene Expression Omnibus (GEO) under the accession number GSE119805. The data that support the findings of this study are available from the corresponding authors upon request.

Supplementary Material

Refer to Web version on PubMed Central for supplementary material.

Acknowledgements

We thank J Dekker, J Gibcus, J Taylor, M Sauria, C Price, J Wolff, M Yukawa, W Deng, and R Perea for advice and/or support during various stages of this project. We thank members of the Namekawa and Kaplan laboratories for discussion and helpful comments regarding the manuscript. Funding sources: Albert J. Ryan Fellowship to K.G.A.; National Institute of Health (NIH) R01 GM098605, R01 GM122776, and R21 ES027117, Research Grant (FY13–510) from the March of Dimes Foundation to S.H.N.; Azrieli Faculty Fellowship and Taub Fellowship to N.K.; NIH DP2 GM119134 to A.B.

References

1. Battulin N et al. Comparison of the three-dimensional organization of sperm and fibroblast genomes using the Hi-C approach. Genome Biol 16, 77 (2015). [PubMed: 25886366]
2. Jung YH et al. Chromatin States in Mouse Sperm Correlate with Embryonic and Adult Regulatory Landscapes. Cell Rep 18, 1366–1382 (2017). [PubMed: 28178516]
3. Du Z et al. Allelic reprogramming of 3D chromatin architecture during early mammalian development. Nature 547, 232–235 (2017). [PubMed: 28703188]
4. Ke Y et al. 3D Chromatin Structures of Mature Gametes and Structural Reprogramming during Mammalian Embryogenesis. Cell 170, 367–381 e20 (2017). [PubMed: 28709003]
5. Hunter N Meiotic Recombination: The Essence of Heredity. Cold Spring Harb Perspect Biol 7(2015).
6. Gray S & Cohen PE Control of Meiotic Crossovers: From Double-Strand Break Formation to Designation. Annu Rev Genet 50, 175–210 (2016). [PubMed: 27648641]
7. Kimmins S & Sassone-Corsi P Chromatin remodelling and epigenetic features of germ cells. Nature 434, 583–9 (2005). [PubMed: 15800613]
8. Schultz N, Hamra FK & Garbers DL A multitude of genes expressed solely in meiotic or postmeiotic spermatogenic cells offers a myriad of contraceptive targets. Proc Natl Acad Sci U S A 100, 12201–6 (2003). [PubMed: 14526100]
9. Namekawa SH et al. Postmeiotic sex chromatin in the male germline of mice. Curr Biol 16, 660–7 (2006). [PubMed: 16581510]
10. Hasegawa K et al. SCML2 Establishes the Male Germline Epigenome through Regulation of Histone H2A Ubiquitination. Dev Cell 32, 574–88 (2015). [PubMed: 25703348]
11. Maezawa S, Yukawa M, Alavattam KG, Barski A & Namekawa SH Dynamic reorganization of open chromatin underlies diverse transcriptomes during spermatogenesis. Nucleic Acids Res 46, 593–608 (2018). [PubMed: 29126117]
12. Soumillon M et al. Cellular source and mechanisms of high transcriptome complexity in the mammalian testis. Cell Rep 3, 2179–90 (2013). [PubMed: 23791531]
13. Maezawa S et al. Polycomb protein SCML2 facilitates H3K27me3 to establish bivalent domains in the male germline. Proc Natl Acad Sci U S A 115, 4957–4962 (2018). [PubMed: 29686098]
14. Dixon JR et al. Topological domains in mammalian genomes identified by analysis of chromatin interactions. Nature 485, 376–80 (2012). [PubMed: 22495300]
15. Nora EP et al. Spatial partitioning of the regulatory landscape of the X-inactivation centre. Nature 485, 381–5 (2012). [PubMed: 22495304]
16. Naumova N et al. Organization of the mitotic chromosome. Science 342, 948–53 (2013). [PubMed: 24200812]
17. Lieberman-Aiden E et al. Comprehensive mapping of long-range interactions reveals folding principles of the human genome. Science 326, 289–93 (2009). [PubMed: 19815776]
18. Fudenberg G & Mirny LA Higher-order chromatin structure: bridging physics and biology. Curr Opin Genet Dev 22, 115–24 (2012). [PubMed: 22360992]
19. Gibcus JH et al. A pathway for mitotic chromosome formation. Science 359(2018).
20. Lajoie BR, Dekker J & Kaplan N The Hitchhiker's guide to Hi-C analysis: practical guidelines. Methods 72, 65–75 (2015). [PubMed: 25448293]
21. Imakaev M et al. Iterative correction of Hi-C data reveals hallmarks of chromosome organization. Nat Methods 9, 999–1003 (2012). [PubMed: 22941365]
22. Flyamer IM et al. Single-nucleus Hi-C reveals unique chromatin reorganization at oocyte-to-zygote transition. Nature 544, 110–114 (2017). [PubMed: 28355183]
23. Nagano T et al. Cell-cycle dynamics of chromosomal organization at single-cell resolution. Nature 547, 61–67 (2017). [PubMed: 28682332]
24. Zickler D & Kleckner N Meiotic chromosomes: integrating structure and function. Annu Rev Genet 33, 603–754 (1999). [PubMed: 10690419]
25. Scherthan H A bouquet makes ends meet. Nat Rev Mol Cell Biol 2, 621–7 (2001). [PubMed: 11483995]

26. Scherthan H, Schofisch K, Dell T & Illner D Contrasting behavior of heterochromatic and euchromatic chromosome portions and pericentric genome separation in pre-bouquet spermatocytes of hybrid mice. Chromosoma 123, 609–24 (2014). [PubMed: 25119530]
27. Dixon JR et al. Chromatin architecture reorganization during stem cell differentiation. Nature 518, 331–6 (2015). [PubMed: 25693564]
28. Javierre BM et al. Lineage-Specific Genome Architecture Links Enhancers and Non-coding Disease Variants to Target Gene Promoters. Cell 167, 1369–1384.e19 (2016). [PubMed: 27863249]
29. Le Dily F et al. Distinct structural transitions of chromatin topological domains correlate with coordinated hormone-induced gene regulation. Genes Dev 28, 2151–62 (2014). [PubMed: 25274727]
30. Wolff J et al. Galaxy HiCExplorer: a web server for reproducible Hi-C data analysis, quality control and visualization. Nucleic Acids Res 46, W11–W16 (2018). [PubMed: 29901812]
31. Ramirez F et al. High-resolution TADs reveal DNA sequences underlying genome organization in flies. Nat Commun 9, 189 (2018). [PubMed: 29335486]
32. Rao SS et al. A 3D map of the human genome at kilobase resolution reveals principles of chromatin looping. Cell 159, 1665–80 (2014). [PubMed: 25497547]
33. Cao Y et al. Accurate loop calling for 3D genomic data with cLoops. bioRxiv (2018).
34. Lesch BJ & Page DC Poised chromatin in the mammalian germ line. Development 141, 3619–26 (2014). [PubMed: 25249456]
35. Turner JM Meiotic sex chromosome inactivation. Development 134, 1823–31 (2007). [PubMed: 17329371]
36. Ichijima Y, Sin HS & Namekawa SH Sex chromosome inactivation in germ cells: emerging roles of DNA damage response pathways. Cell Mol Life Sci 69, 2559–72 (2012). [PubMed: 22382926]
37. Deng X et al. Bipartite structure of the inactive mouse X chromosome. Genome Biol 16, 152 (2015). [PubMed: 26248554]
38. Giorgetti L et al. Structural organization of the inactive X chromosome in the mouse. Nature 535, 575–9 (2016). [PubMed: 27437574]
39. Minajigi A et al. Chromosomes. A comprehensive Xist interactome reveals cohesin repulsion and an RNA-directed chromosome conformation. Science 349(2015).
40. Wang CY, Jegu T, Chu HP, Oh HJ & Lee JT SMCHD1 Merges Chromosome Compartments and Assists Formation of Super-Structures on the Inactive X. Cell 174, 406–421.e25 (2018). [PubMed: 29887375]
41. Namekawa SH, Payer B, Huynh KD, Jaenisch R & Lee JT Two-step imprinted X inactivation: repeat versus genic silencing in the mouse. Mol Cell Biol 30, 3187–205 (2010). [PubMed: 20404085]
42. Sin HS, Ichijima Y, Koh E, Namiki M & Namekawa SH Human postmeiotic sex chromatin and its impact on sex chromosome evolution. Genome Res 22, 827–36 (2012). [PubMed: 22375025]
43. Liang Z et al. Chromosomes Progress to Metaphase in Multiple Discrete Steps via Global Compaction/Expansion Cycles. Cell 161, 1124–1137 (2015). [PubMed: 26000485]
44. Dekker J, Rippe K, Dekker M & Kleckner N Capturing chromosome conformation. Science 295, 1306–11 (2002). [PubMed: 11847345]
45. Schalbetter SA, Fudenberg G, Baxter J, Pollard KS & Neale MJ Principles of Meiotic Chromosome Assembly. bioRxiv (2018).
46. Muller H et al. Characterizing meiotic chromosomes' structure and pairing using a designer sequence optimized for Hi-C. Mol Syst Biol 14, e8293 (2018). [PubMed: 30012718]
47. Duan Z et al. A three-dimensional model of the yeast genome. Nature 465, 363–7 (2010). [PubMed: 20436457]
48. Mizuguchi T et al. Cohesin-dependent globules and heterochromatin shape 3D genome architecture in S. pombe. Nature 516, 432–435 (2014). [PubMed: 25307058]
49. Tjong H, Gong K, Chen L & Alber F Physical tethering and volume exclusion determine higher-order genome organization in budding yeast. Genome Res 22, 1295–305 (2012). [PubMed: 22619363]

50. Rao SSP et al. Cohesin Loss Eliminates All Loop Domains. Cell 171, 305–320.e24 (2017). [PubMed: 28985562]
51. Haarhuis JHI et al. The Cohesin Release Factor WAPL Restricts Chromatin Loop Extension. Cell 169, 693–707.e14 (2017). [PubMed: 28475897]
52. Busslinger GA et al. Cohesin is positioned in mammalian genomes by transcription, CTCF and Wapl. Nature 544, 503–507 (2017). [PubMed: 28424523]
53. McNicoll F, Stevense M & Jessberger R Cohesin in gametogenesis. Curr Top Dev Biol 102, 1–34 (2013). [PubMed: 23287028]
54. Loukinov DI et al. BORIS, a novel male germ-line-specific protein associated with epigenetic reprogramming events, shares the same 11-zinc-finger domain with CTCF, the insulator protein involved in reading imprinting marks in the soma. Proc Natl Acad Sci U S A 99, 6806–11 (2002). [PubMed: 12011441]
55. Bergeron-Sandoval LP, Safaee N & Michnick SW Mechanisms and Consequences of Macromolecular Phase Separation. Cell 165, 1067–1079 (2016). [PubMed: 27203111]
56. Banani SF, Lee HO, Hyman AA & Rosen MK Biomolecular condensates: organizers of cellular biochemistry. Nat Rev Mol Cell Biol 18, 285–298 (2017). [PubMed: 28225081]
57. Larson AG et al. Liquid droplet formation by HP1alpha suggests a role for phase separation in heterochromatin. Nature 547, 236–240 (2017). [PubMed: 28636604]
58. Strom AR et al. Phase separation drives heterochromatin domain formation. Nature 547, 241–245 (2017). [PubMed: 28636597]
59. Hnisz D, Shrinivas K, Young RA, Chakraborty AK & Sharp PA A Phase Separation Model for Transcriptional Control. Cell 169, 13–23 (2017). [PubMed: 28340338]
60. Holliday R The biological significance of meiosis. Symp Soc Exp Biol 38, 381–94 (1984). [PubMed: 6400219]
61. Bellve AR Purification, culture, and fractionation of spermatogenic cells. Methods Enzymol 225, 84–113 (1993). [PubMed: 8231890]
62. Hasegawa K et al. SCML2 establishes the male germline epigenome through regulation of histone H2A ubiquitination. Dev Cell 32, 574–88 (2015). [PubMed: 25703348]
63. Maezawa S, Yukawa M, Alavattam KG, Barski A & Namekawa SH Dynamic reorganization of open chromatin underlies diverse transcriptomes during spermatogenesis. Nucleic Acids Res 46, 593–608 (2018). [PubMed: 29126117]
64. Maezawa S et al. Polycomb protein SCML2 facilitates H3K27me3 to establish bivalent domains in the male germline. Proc Natl Acad Sci U S A 115, 4957–4962 (2018). [PubMed: 29686098]
65. Schindelin J et al. Fiji: an open-source platform for biological-image analysis. Nat Methods 9, 676–82 (2012). [PubMed: 22743772]
66. Schneider CA, Rasband WS & Eliceiri KW NIH Image to ImageJ: 25 years of image analysis. Nat Methods 9, 671–5 (2012). [PubMed: 22930834]
67. Belaghzal H, Dekker J & Gibcus JH Hi-C 2.0: An optimized Hi-C procedure for high-resolution genome-wide mapping of chromosome conformation. Methods 123, 56–65 (2017). [PubMed: 28435001]
68. Rao SS et al. A 3D map of the human genome at kilobase resolution reveals principles of chromatin looping. Cell 159, 1665–80 (2014). [PubMed: 25497547]
69. Lajoie BR, Dekker J & Kaplan N The Hitchhiker's guide to Hi-C analysis: practical guidelines. Methods 72, 65–75 (2015). [PubMed: 25448293]
70. Jung YH et al. Chromatin States in Mouse Sperm Correlate with Embryonic and Adult Regulatory Landscapes. Cell Rep 18, 1366–1382 (2017). [PubMed: 28178516]
71. Selvaraj S, J, R.D., Bansal, V. & Ren, B. Whole-genome haplotype reconstruction using proximity-ligation and shotgun sequencing. Nat Biotechnol 31, 1111–8 (2013). [PubMed: 24185094]
72. Naumova N et al. Organization of the mitotic chromosome. Science 342, 948–53 (2013). [PubMed: 24200812]
73. Du Z et al. Allelic reprogramming of 3D chromatin architecture during early mammalian development. Nature 547, 232–235 (2017). [PubMed: 28703188]

74. Imakaev M et al. Iterative correction of Hi-C data reveals hallmarks of chromosome organization. Nat Methods 9, 999–1003 (2012). [PubMed: 22941365]
75. Abdennur N, Goloborodko A, Imakaev M, & Mirny L mirnylab/cooler: v0.7.10. doi:10.5281/zenodo.1243296 (2018).
76. Langmead B & Salzberg SL Fast gapped-read alignment with Bowtie 2. Nat Methods 9, 357–9 (2012). [PubMed: 22388286]
77. Ramirez F et al. High-resolution TADs reveal DNA sequences underlying genome organization in flies. Nat Commun 9, 189 (2018). [PubMed: 29335486]
78. Wolff J et al. Galaxy HiCExplorer: a web server for reproducible Hi-C data analysis, quality control and visualization. Nucleic Acids Res 46, W11–W16 (2018). [PubMed: 29901812]
79. Kaplan N & Dekker J High-throughput genome scaffolding from in vivo DNA interaction frequency. Nat Biotechnol 31, 1143–7 (2013). [PubMed: 24270850]
80. Virkar Y & Clauset A Power-law distributions in binned empirical data. Ann. Appl. Stat. 8, 89–119 (2014).
81. Oliphant TE Python for Scientific Computing. Computing in Science & Engineering 9, 10–20 (2007).
82. Lieberman-Aiden E et al. Comprehensive mapping of long-range interactions reveals folding principles of the human genome. Science 326, 289–93 (2009). [PubMed: 19815776]
83. Crane E et al. Condensin-driven remodelling of X chromosome topology during dosage compensation. Nature 523, 240–4 (2015). [PubMed: 26030525]
84. Zhang Y et al. Spatial organization of the mouse genome and its role in recurrent chromosomal translocations. Cell 148, 908–21 (2012). [PubMed: 22341456]
85. Ramirez F et al. High-Affinity Sites Form an Interaction Network to Facilitate Spreading of the MSL Complex across the X Chromosome in Drosophila. Mol Cell 60, 146–62 (2015). [PubMed: 26431028]
86. Khan A & Mathelier A Intervene: a tool for intersection and visualization of multiple gene or genomic region sets. BMC Bioinformatics 18, 287 (2017). [PubMed: 28569135]
87. Conway JR, Lex A & Gehlenborg N UpSetR: an R package for the visualization of intersecting sets and their properties. Bioinformatics 33, 2938–2940 (2017). [PubMed: 28645171]
88. Cao Y et al. Accurate loop calling for 3D genomic data with cLoops. bioRxiv (2018).
89. Kobayashi H et al. Contribution of intragenic DNA methylation in mouse gametic DNA methylomes to establish oocyte-specific heritable marks. PLoS Genet 8, e1002440 (2012). [PubMed: 22242016]
90. Adams SR et al. RNF8 and SCML2 cooperate to regulate ubiquitination and H3K27 acetylation for escape gene activation on the sex chromosomes. PLoS Genet 14, e1007233 (2018). [PubMed: 29462142]
91. Shen Y et al. A map of the cis-regulatory sequences in the mouse genome. Nature 488, 116–20 (2012). [PubMed: 22763441]
92. Dowen JM et al. Control of cell identity genes occurs in insulated neighborhoods in mammalian chromosomes. Cell 159, 374–387 (2014). [PubMed: 25303531]
93. Dobin A et al. STAR: ultrafast universal RNA-seq aligner. Bioinformatics 29, 15–21 (2013). [PubMed: 23104886]
94. Langmead B, Trapnell C, Pop M & Salzberg SL Ultrafast and memory-efficient alignment of short DNA sequences to the human genome. Genome Biol 10, R25 (2009). [PubMed: 19261174]
95. Zhang Y et al. Model-based analysis of ChIP-Seq (MACS). Genome Biol 9, R137 (2008). [PubMed: 18798982]
96. Kartashov AV & Barski A BioWardrobe: an integrated platform for analysis of epigenomics and transcriptomics data. Genome Biol 16, 158 (2015). [PubMed: 26248465]
97. Kent WJ et al. The human genome browser at UCSC. Genome Res 12, 996–1006 (2002). [PubMed: 12045153]
98. Ramirez F et al. deepTools2: a next generation web server for deep-sequencing data analysis. Nucleic Acids Res 44, W160–5 (2016). [PubMed: 27079975]

99. Shen L, Shao N, Liu X & Nestler E ngs.plot: Quick mining and visualization of next-generation sequencing data by integrating genomic databases. BMC Genomics 15, 284 (2014). [PubMed: 24735413]

100. Quinlan AR BEDTools: The Swiss-Army Tool for Genome Feature Analysis. Curr Protoc Bioinformatics 47, 11 12 1–34 (2014). [PubMed: 25199789]

101. Hadley W Ggplot2, pages cm (Springer Science+Business Media, LLC, New York, NY, 2016).

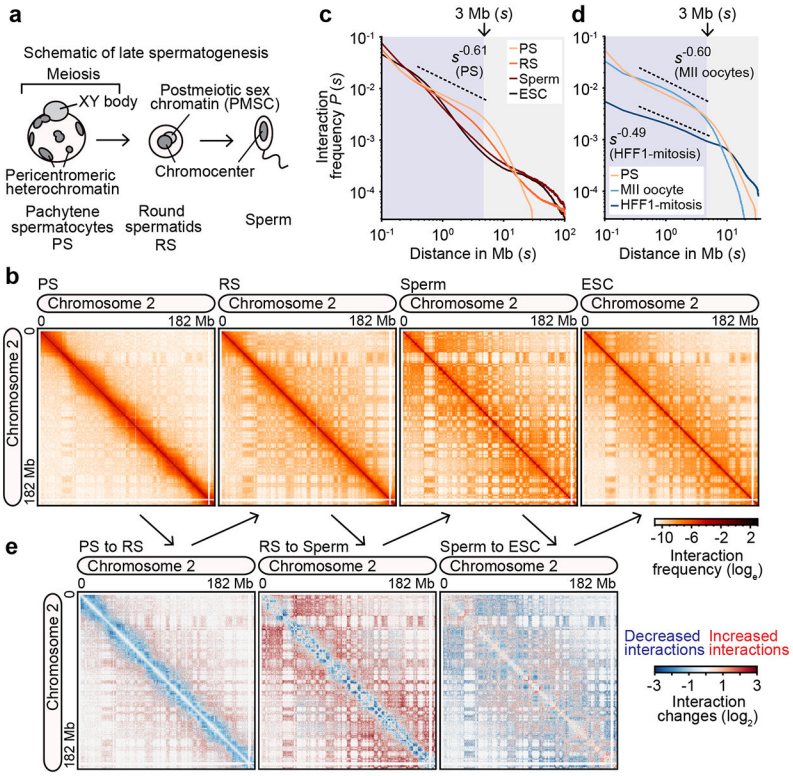

Figure 1. Dynamic 3D chromatin organization in late spermatogenesis.

a, Schematic of stages of late spermatogenesis analyzed in this study. PS: pachytene spermatocyte; RS: round spermatid. **b**, Heatmaps showing normalized Hi-C interaction frequencies (128-kb bins, chromosome 2) in PS, RS, sperm, and embryonic stem cells (ESC). **c**, **d**, Hi-C intrachromosomal interaction frequency probabilities *P* stratified by genomic distance *s* for each cell type shown in the panels (100-kb bins, all chromosomes). MII oocyte: metaphase meiosis II oocyte; HFF1-mitosis: synchronized prometaphase mitosis human foreskin fibroblasts. The blue shadow indicates intrachromosomal interactions up to 3 Mb, and the grey shadow indicates intrachromosomal interactions at and beyond 3 Mb. Scaling coefficients are shown in the panels. **e**, $\log_2$ ratio comparisons of the Hi-C interaction frequencies (128-kb bins, chromosome 2) for successive cell types. Details and metrics for Hi-C datasets are presented in Supplementary Dataset 2.

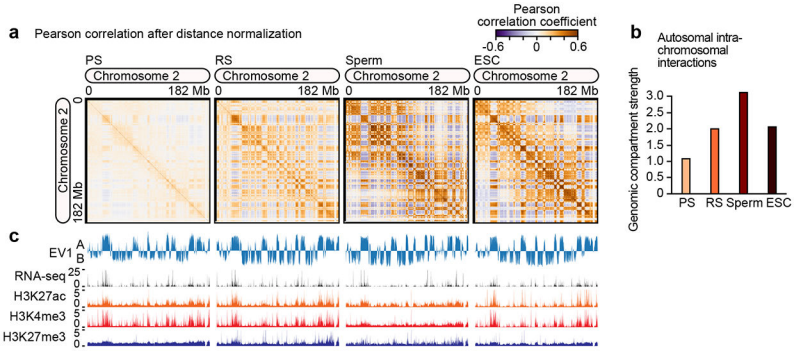

Figure 2. Attenuated compartmentalization of 3D chromatin organization in meiosis and its maturation in sperm development.

a, Pearson's correlation for Hi-C interaction frequencies (128-kb bins, chromosome 2), which captures genomic compartmentalization patterns in pachytene spermatocytes (PS), round spermatids (RS), sperm, and embryonic stem cells (ESC). **b**, Autosomal intrachromosomal interactions determined by the measurement of genomic compartment strength (Methods). **c**, Eigenvector 1 (EV1) from principle component analysis, RNA-seq data, and ChIP-seq data for H3K27ac, H3K4me3, and H3K27me3 to classify genomic compartments as active (A) and repressed (B) in all cell types (128-kb bins, chromosome 2). First eigenvectors from principle component analysis are presented in Supplementary Dataset 3.

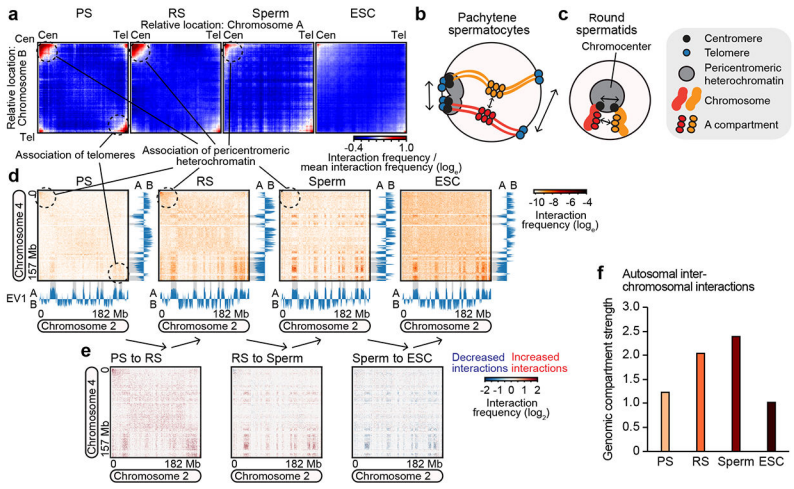

Figure 3. Interchromosomal interactions in late spermatogenesis.

a, Average interchromosomal interactions between different chromosomes (denoted as chromosome A and chromosome B; Methods) in pachytene spermatocytes (PS), round spermatids (RS), sperm, and embryonic stem cells (ESC). Cen: acrocentric ends (telomeres proximal to centromeres); Tel: non-centromeric ends (telomeres distal to centromeres). **b**, **c**, Models of interchromosomal interactions in pachytene spermatocytes (**b**) and round spermatids (**c**). **d**, Heatmaps showing normalized Hi-C interchromosomal interactions (250-kb bins, chromosomes 2 and 4) for all cell types. **e**, $\log_2$ ratio comparisons of the interchromosomal interaction frequencies (250-kb bins, chromosomes 2 and 4) for successive cell types. **f**, Autosomal interchromosomal interactions determined by measurements of genomic compartment strength (Methods). First eigenvectors from principle component analysis are presented in Supplementary Dataset 3.

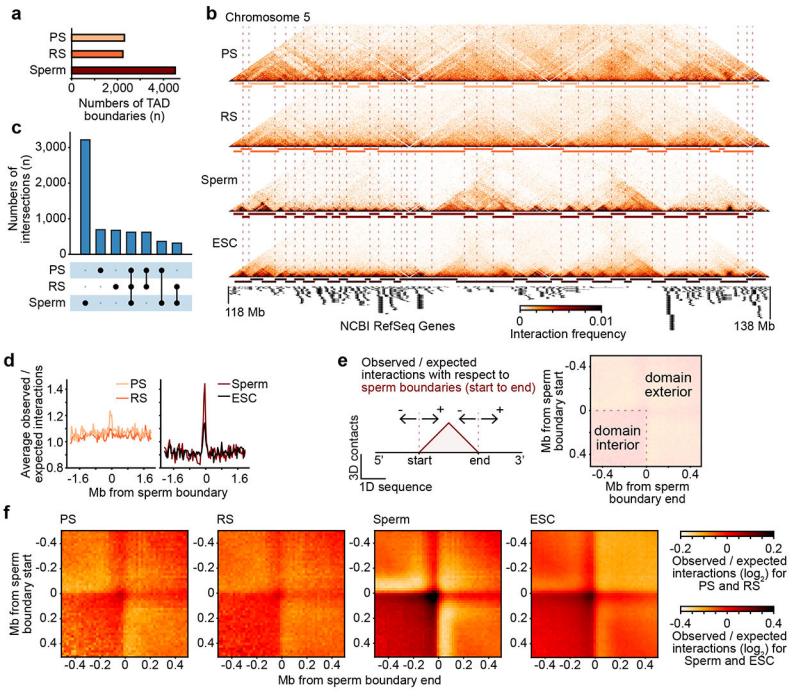

Figure 4. Attenuated topologically associating domains in meiosis and their maturation in sperm development.

a, Numbers of TAD boundaries (n) in each dataset (60 kb centered on the boundary, 20-kb bins) for pachytene spermatocytes (PS), round spermatids (RS), and sperm. **b**, Hi-C interaction heatmaps (20-kb bins, chromosome 5, 118-138 Mb) showing dynamics of local interactions, and TADs in PS, RS, sperm, and embryonic stem cells (ESC). Horizontal solid bars: TADs as delimited by the software package HiCExplorer (Methods); dashed transparent bars: sperm TAD start and stop boundaries. **c**, Numbers of intersections of TAD boundaries (n) between datasets. Vertical bars: Overlap between TAD boundaries in the datasets below, which are further specified by solid black circles; black lines connecting the black circles indicate overlaps between multiple datasets. The intersections were plotted using the Intervene and UpSetR packages (Methods). **d**, Average observed/expected interaction frequencies at sperm TAD boundaries ± 2 Mb for all cell types (20-kb bins, chromosome 2). **e**, Schematic for interpretation of 2D matrix visualizations of observed/expected interaction frequencies at sperm TAD start and stop boundaries. **f**, 2D matrix visualizations of $\log_2$ observed/expected interaction frequencies at sperm TAD start and stop boundaries ± 0.5 Mb for all cell types (20-kb bins, all chromosomes). Genomic location information for TAD boundaries and results from the evaluation of TAD boundary intersections are presented in Supplementary Dataset 4.

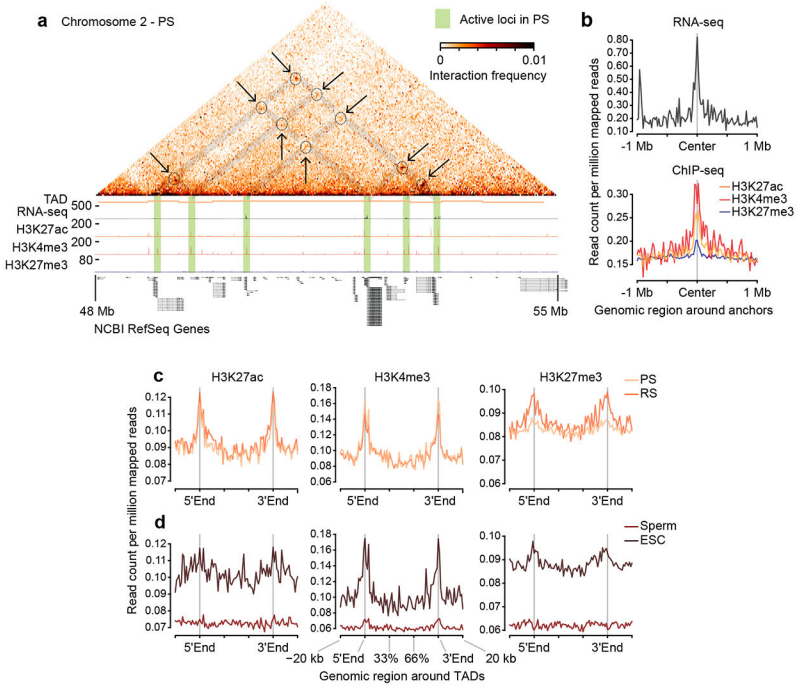

Figure 5. Pairwise point interactions and sperm TADs are delineated with epigenetic marks.

a, Hi-C interaction heatmaps (20-kb bins, chromosome 2, 48-55 Mb) of pachytene spermatocytes (PS) showing the dynamics of local interactions of active gene loci together with RNA-seq data and ChIP-seq data for H3K27ac, H3K4me3, and H3K27me3. y axis: RPKM. Solid bars: TADs called by the HiCExplorer application hicFindTADs (Methods). Green and grey highlights, arrows, and dashed circles indicate localized pairwise point interactions and related features of interest. **b**, RNA-seq data (top) and ChIP-seq data for H3K27ac, H3K4me3, and H3K27me3 (bottom) to examine enrichment at the center of pachytene spermatocyte point interaction anchors ± 1 Mb (20-kb bins, all chromosomes). Point interactions were called with the software package cLoops (Methods). **c**, **d**, ChIP-seq data for H3K27ac, H3K4me3, and H3K27me3 to examine enrichment at sperm TAD start and stop boundaries along with domain interior and exterior (± 20 kb) portions (20-kb bins, all autosomes), in pachytene spermatocytes (PS), round spermatids (RS), sperm, and embryonic stem cells (ESC). Genomic location information for pairwise point interactions are presented in Supplementary Dataset 5.

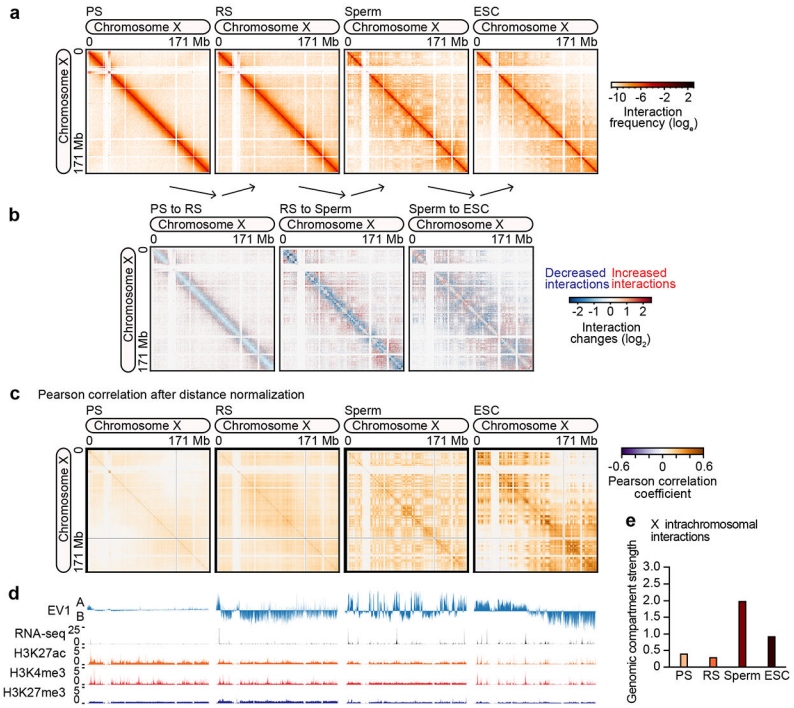

Figure 6. Chromosome X lacks higher-order structure during meiotic and postmeitoic silencing.

a, Heatmaps showing normalized Hi-C interaction frequencies (128-kb bins, chromosome X) in pachytene spermatocytes (PS), round spermatids (RS), sperm, and embryonic stem cells (ESC). **b**, $\log_2$ ratio comparisons between the Hi-C interaction frequencies for successive cell types (128-kb bins, chromosome X). **c**, Pearson's correlation for Hi-C interaction frequencies (128-kb bins, chromosome X), which captures genomic compartmentalization patterns in all cell types. **d**, Eigenvector 1 (EV1) from principle component analysis, RNA-seq data, and ChIP-seq data for H3K27ac, H3K4me3, and H3K27me3 to classify genomic compartments as active (A) and repressed (B) in all cell types (128-kb bins, chromosome X). **e**, X intrachromosomal interactions determined by the measurement of genomic compartment strength (Methods). First eigenvectors from principle component analysis are presented in Supplementary Dataset 3.